Length and polarity dependent saturation of the electromechanical response of piezoelectric semiconducting nanowires

Andrés Jenaro Lopez Garcia, Mireille Mouis, Thomas Jalabert, Alessandro Cresti, Gustavo Ardila

Length and polarity dependent saturation of the electromechanical response of piezoelectric semiconducting nanowires

Authors: Andrés Jenaro Lopez Garcia, Mireille Mouis, Thomas Jalabert, Alessandro Cresti, Gustavo Ardila

Univ. Grenoble Alpes, Univ. Savoie Mont Blanc, CNRS, Grenoble INP, IMEP-LaHC, F-38000 Grenoble, FRANCE
E-mail: mouis@minatec.grenoble-inp.fr, ardilarg@minatec.grenoble-inp.fr

Keywords: Semiconducting piezoelectric nanowire, Surface traps, Surface Fermi level pinning, Finite Element modelling, Analytical modelling, Electromechanical transducers, Nanogenerator

Abstract:

The question of the length dependence of the electromechanical response of semiconducting piezoelectric NWs was explored. We identified a new physical mechanism of piezoresponse saturation, which originates from the combination of the influence of interface traps and piezoelectric polarization in the depleted NW. Our results are in better qualitative agreement with experimental observations than presently existing theories. To do so, we used the Finite Element Method to simulate the coupled set of equations describing mechanical, piezoelectric and semiconducting properties. In order to reduce the number of parameters, simulations focused on the case of uniform ZnO nanowires grown along the c-axis. Saturation was explained by the incapacity of surface traps to maintain depletion along the whole NW beyond a certain length, as a result of the electric potential shift induced by piezoelectric polarization. An analytical model was developed to support this analysis. It provided the dependence trends of saturation length and piezoresponse as a function of NW dimensions, doping level, surface traps density and crystal polarity, as well as with external pressure, in fair agreement with simulation results. Moreover, we discovered that one consequence of this mechanism was that crystal polarity had an impact on the smoothness of the radius-dependent transition between high and low piezoresponse under axial stress. These results have important implications for the optimization of electromechanical sensors and nanogenerators based on piezoelectric semiconducting NWs and related composite materials.

1. Introduction

The bulk piezoelectric properties of semiconducting (SC) piezoelectric materials such as ZnO or III- nitrides may seem less appealing than those of the best piezoelectric ceramics, due to screening by free carriers. However, they have the advantage of being free of toxic or critical materials such as lead, barium or bismuth, which are used in many high performance piezoelectric ceramics.[1][2] Moreover they can be easily grown at low temperature in the form of vertical wurtzite crystalline nanowires (NWs), with their preferential orientation along the polarized c-axis.[3][4] This nanostructuration has several advantages. Piezoelectric SC NWs do not need to be poled and can be integrated on a wide variety of substrates, from silicon substrates – for potential above-IC integration on CMOS – to flexible and conformal substrates such as stainless steel or polymer foils, thus opening a wide range of applications.[5] Moreover, there is a growing consensus about the fact that their piezoelectric performance is improved by nanostructuration, and it is the aim of this paper to clarify the physical mechanisms that underline this improvement.

It should be noted that energy conversion efficiency between input and output energies is probably the most meaningful parameter to characterize performance in terms of applications. However, it has the drawback of depending on experimental details, such as electrical load circuit or operation mode – input energy being mechanical energy for mechanical sensors or mechanical energy harvesters, and electrical energy for Piezoelectric Force Microscopy (PFM), for instance. In order to make comparisons easier, the performance of piezoelectric devices and materials is thus often characterized by more intrinsic parameters, among which the open circuit potential (V_{OC}) and the piezoelectric coefficients (mainly d_{ij}, and especially d_{33} which correlates strain and electric field along c-axis). In this paper, we will discuss V_{OC}, which is a directly measurable parameter. It should be noted that d_{33} can be deduced from V_{OC} with the additional knowledge of device capacitance.[6] The trends obtained here for V_{OC} can be directly extrapolated to piezoelectric coefficients such as d_{33} since we are interested only in NW geometry-related effects and materials are kept the same.

Several devices that implement vertical NW arrays have successfully exploited the properties of nanostructured SC piezoelectric materials, among which the Vertically Integrated NanoGenerator (VING) is one of the most studied. It has evolved since the first demonstration [7] and is now based on a composite layer sandwiched between two metallic contacts. The composite layer consists in a

NW array grown on a substrate, embedded in a matrix material and capped by an insulating layer.[8]

Strikingly, these devices are much more efficient than what would be expected with the residual doping levels of present growth methods. Indeed, ZnO is known to be unintentionally highly N-type doped.[3][9][10]. However, high doping results in degraded piezoelectric properties due to polarization screening by free electrons. The resulting correlation between piezoelectric properties and carriers concentration has been identified for long in bulk materials.[11],[12] Similar correlations have been found in nanorods [13] and attributed to variations in impurity incorporation during the solution growth. Doping compensation was found to improve NW performance [14]. The influence of doping level on the piezoelectric performance of SC NWs has been preferably explored in materials such as GaN due to easier control than in ZnO. It has been firstly studied directly at device level, by comparing V_{OC} values produced by VING devices that included GaN NW arrays obtained by plasma-assisted molecular beam epitaxy (PA-MBE), with different levels of Si doping.[15] A clear correlation has been found with carrier concentration, with a peak potential that decreased from 80 mV to about 5 mV for electron concentrations, deduced from Raman scattering measurements, which increased from 8×10^{17} cm^{-3} to 1.5×10^{19} cm^{-3}, respectively. A first attempt to evaluate the role of doping level on the piezoresponse of ZnO has been made by comparing the piezoresponse of ZnO NWs grown by 2 different techniques, namely the high temperature Vapor-Liquid-Solid (VLS) and the low temperature Aqueous Chemical Growth (ACG) methods.[16] The piezoresponse has been analyzed by scanning a conducting Atomic Force Microscope (AFM) tip at given height over the NW array, so that the tip measured the electrical signal generated while it bended and released each NW it encountered. A clear difference has been obtained between the VLS and ACG grown arrays, which produced a mean potential in the range of 30 mV-35 mV and around 5 mV, respectively. It has been attributed to the higher residual doping obtained with ACG, with possibly an additional contribution of bending limitations due to the larger density of NWs on these ACG samples. More recently, this effect has been explored in a more quantitative way for ZnO NWs fabricated by Chemical Bath Deposition (CBD) with different levels of Ga or Al doping using a combination of Scanning Spreading Resistance Microscopy (SSRM) and Piezoelectric Force Microscopy (PFM) in order to evaluate carrier concentration and piezoelectric response, respectively.[17] The PFM amplitude was divided by 2,

from about 80 pm for non-intentionally Ga doped ZnO to about 40 pm for carrier concentrations above 2×10^{19} cm^{-3}.

All these values are much larger than what would be expected from highly doped SC. It is therefore clear that some other effects than in bulk materials need to be included in order to explain the results obtained experimentally with NWs. In particular, geometry has been found to play a key role. Indeed, it has recently been explained that the performance enhancement brought by nanostructuration could be linked to the presence of large densities of traps at the surface of ZnO, or at its interface with the surrounding materials when NWs are embedded in a matrix.[18] This assumption of large surface traps densities is fully consistent with the Fermi level pinning which typically occurs at the surface of these SC materials[19], and the large piezoresponse obtained experimentally cannot be reconciled with present residual levels of doping without accounting for a certain amount of slow surface traps.[20].

Within this conceptual framework, the influence of NW diameter and doping level starts to be rather well understood. From a theoretical point of view, the diameter dependence of piezoelectric response has been shown to result from the competition between the screening of strain-induced polarization by free carriers (free electrons in the case of N-type SC) and surface depletion by surface traps.[18][21] As a result, the NW piezoelectric response varies between two extreme values: a maximum value corresponding to that of a fully depleted NW below a critical radius R_{cr}, and a minimum value corresponding to that of a thin film above R_{cr}. The transition between the 2 regimes has been found to be quite sharp. The critical radius/diameter depends on doping level and surface trap density (see Supporting Information for analytical expression in cylindrical coordinates under the full depletion approximation). With critical diameters in the range of several tens of nanometers, which can be easily achieved experimentally,[21] efficient piezopotential generation is indeed under reach, even for doping levels beyond $10^{18}cm^{-3}$, provided a sufficient amount of slow traps is present.[20] The use of core/shell structures with a radial PN junction has been shown to allow band bending control, thus increasing the range of available diameters for a given doping level in the core [22],[23]. However, these techniques do not suppress all the issues related to free carrier screening. In the following, we will concentrate on uniformly doped SC NWs, in order to limit the number of parameters and keep the focus on the fundamental physical phenomena involved.

Experimentally, beyond literature surveys which can only provide indirect and qualitative clues due to the large number of interfering parameters, the influence of geometry on NW piezoresponse has only started to be examined quantitatively. In a recent paper,[24] vertical GaN NWs with light P-doping, sub-100 nm diameters and about 1 µm length have been grown by PA-MBE and their piezoelectric properties tested at nanoscale by measuring simultaneously the open circuit voltage V_{OC} and the deformation under controlled vertical force. Results corresponding to purely axial compression have been obtained with the "rigid NWs" population. An increase of piezo-conversion efficiency has been seen, which is consistent with the above-mentioned explanation by surface traps, with surface Fermi level pinning and subsequent full depletion of thin enough NWs.[18] Surface depletion effects have also been invoked to explain the significant response that has been obtained on highly doped GaN and ZnO NWs, as a result of the large density of surface traps (a few $10^{13}cm^{-2}$) associated with the growth method.[17] Some results have also been obtained by PFM. The statistical exploitation of the PFM amplitude obtained on the top surface of the NWs grown on different gravure-printed seed layers has brought out the conclusion that a larger response was obtained from narrower NWs, with 25 pm and 20 pm average values obtained for 100 nm and 200 nm radius, respectively.[25] The increase of piezoelectric response and effective piezoelectric coefficient from narrower NWs has been found consistent with the theoretical values predicted by FEM for doping levels of several 10^{17} cm-3 and surface traps densities in the range of 10^{12} $eV^{-1}cm^{-2}$ to 10^{13} $eV^{-1}cm^{-2}$.[26]

While diameter influence starts to be understood, the influence of NW length has been much less explored. The performance of ZnO VING structures fabricated using a polyester textile as substrate and bottom electrode has shown a significant improvement of performance with NW length, with average V_{OC} increasing from 0.43 V to 0.66 V and 1.32 V as NW length increased from 2.3 µm to 3.9 µm and 5.9 µm, respectively.[27] However, in this experiment, performance has been measured by shaking the samples at given frequency, so that longer NWs may have a larger latitude to move at their top and the improvement cannot be ascribed to purely geometrical effects. An increase of V_{OC} with NW length has also been observed in GaN NW-based VINGs, with output voltage increasing from 6.7V to 13.1V and 18.7V as NW length increased from 4.5µm to 9.4µm and 14.5µm, respectively.[28] It should be noted that in this device, an additional NiO layer was used in order to introduce a PN junction at the top of the NWs. In terms of models, the dominant picture, which stems from insulating NW models, is often that the piezoresponse is proportional to

length for given pressure. Nonetheless, semiconducting effects have been accounted for by Romano et al. using FEM simulations of axially strained NWs under the assumption of ideal interfaces without surface traps.[29] It has been concluded that piezopotential would saturate at very small values, as the polarization field would be screened everywhere, except in a thin strain-induced depletion region at the very top of the NW.[29] It should then be useless to grow long NWs, especially with large residual doping levels. A more nuanced analyze, also based on FEM simulations, can be found in [21] where surface traps have been included. A length-dependent saturation has been found as well, although for much longer NWs than in [29] (several microns instead of a few nanometers with doping levels in the $10^{18}cm^{-3}$ range) and with an influence of crystal polarity. However, in that paper, no explanation has been provided.

Thus, it is the aim of this paper to verify the existence of a length-dependent saturation of the piezoresponse in semiconducting piezoelectric NWs, and to provide a consistent understanding of this phenomenon. The analysis was based on FEM simulations of a unit cell that is representative of typical VING devices. Piezoresponse was found to saturate for NW lengths above a critical value, although the saturation mechanism was deeply different from the one identified by Romano et al.[29] In order to support our explanation of the mechanism behind this saturation, we developed an analytical model of V_{OC}. It allowed discussing the influence of doping level, traps density and NW diameter on critical length and V_{OC} saturation values. Length saturation will be reported firstly for O-polar crystalline orientation, while the differences brought by Zn-polar orientation will be discussed in a following section. In order to reduce the number of parameters, simulations were focused on uniform ZnO NWs grown along the c-axis.

2. Device under study

For this study, we used a classical VING structure configuration. Fig. 1 shows a typical implementation on a stainless steel foil substrate, which provides the bottom contact. Rigid substrates, such as silicon, can be found as well. The active layer consisted of an array of vertical n-type ZnO NWs immerged in a dielectric matrix which provided mechanical robustness (yellow region). A thin ZnO seed layer (in red) was deposited on the substrate to promote NW growth. Polymethyl methacrylate (PMMA) was used as matrix material. The active layer was separated from top contact (in green) by an insulating capping layer (in blue) made of the same material as the matrix material. Details about the process can be found in [30].

This type of device is usually used in vertical compression mode on rigid substrates. If integrated on a flexible substrate it can also be used in bending mode. This kind of deformation results in lateral stretching or compression if the active layer is integrated sufficiently far from the neutral plane. Due to material anisotropy, the piezopotential would also be generated along NW axis, although with a different efficiency depending on mechanical properties of matrix material and capping layer, and with the possibility of obtaining negative (compressive) or positive (stretching) axial strains.[31]. In this paper, we will focus on pure axial vertical compression.

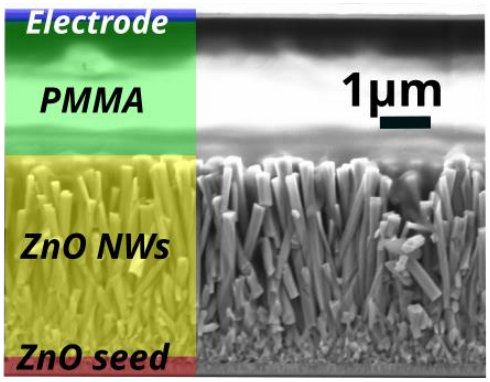

Fig. 1 SEM image of a typical VING device based on ZnO NWs grown on Si substrate by using CBD above a seed layer grown by Atomic Layer Deposition (ALD).

VING devices operate in capacitive mode, a displacement current being generated across the external circuit in order to neutralize the charge unbalance created by the modification of piezoelectric polarization that follows a change in mechanical load. Ideally, there are no leakage currents, and thus no conduction current contributions. As a result, the VING response to repetitive press and release actions consists in a succession of positive and negative current and voltage peaks, the amplitude of which depends on the characteristics of the external circuit. The open circuit voltage (V_{OC}) is often used to make comparisons easier. Numerically, it can be calculated as the variation of potential that results from a change in mechanical load.

3. Simulation framework

In this work, we used a Finite Element Method (FEM) approach to simulate the full set of differential equations that couple mechanical, piezoelectric and semiconducting properties. Simulations were carried out with the *Solid Mechanics* and *Electrostatic* modules of Comsol Multiphysics® software, with the inclusion of piezoelectric electromechanical coupling, and with

the addition of user-defined equations that account for the semiconducting properties of ZnO, with position dependent surface and space charge densities (specified in next sections). The anisotropy of mechanical and piezoelectric properties was accounted for. The meshing was controlled in order to guarantee that it was fine enough in large gradient areas and that the meshes were keeping a correct aspect-ratio (see Supporting Information for the parameters used for the tensors and for an example of meshing). As in previous works, we performed static simulations [18], the piezoresponse being evaluated by V_{OC}, which was calculated as the difference between two simulations accounting for initial and final mechanical load conditions, respectively. V_{OC} (positive or negative) corresponds to the maximum amplitude that can be expected for the voltage peaks in response to the application or to the release of an external pressure on VING top surface. In order to account for Fermi level pining effects, we introduced traps at ZnO/PMMA interfaces,. Traps distribution in SC bandgaps can vary depending on the materials involved and on processing details. In the absence of more precise information, we assumed a uniform density of traps. As in [18], we considered the case of slow traps, which were thus assumed to retain their initial equilibrium electric charge. The surface charge density σ_s at ZnO surface was written as a function of the local potential calculated in the initial state. σ_s was thus position-dependent but time-invariant.

3.1. Simulated structure

In this paper, we considered ZnO as a typical example of semiconducting piezoelectric material. The results can be easily transposed to other materials using proper parameters. The simulated structure consisted in one vertical ZnO NW on its ZnO seed layer, PMMA matrix material and cap layer, and bottom and top contacts. It can be viewed as the typical unit cell of a VING device. The geometry was simplified by using a 2D axisymmetric representation, which was verified to provide negligible error compared to the full 3D simulation of hexagonal shaped NWs, in comparison with the uncertainties about experimental values of doping level and traps densities. In all simulations, the initial and final states corresponded to 0 MPa and -1 MPa external pressure (downwards pressure on top surface). The seed and capping layers were 100 nm thick. Since this paper is focusing on geometry and crystal polarity dependent effects, the values of doping level and traps density used in FEM simulations were taken constant all over the paper, with $N_d = 5\times10^{17}$ cm-3 and $N_{it} = 10^{13}$ $eV^{-1}cm^{-2}$, unless explicitly stated otherwise. These values are quite representative of what can be obtained using CBD, for instance.[21] Note that the possible difference of doping level

associated to O-polar and Zn-polar growth was not accounted for, in order to clearly decorrelate doping and geometry effects. NW radius and length, as well as crystal polarity, were varied. The radius of the simulated domain was twice the NW radius. The relative permittivity and bandgap of ZnO were equal to ε_r=8.91 and E_g=3.37eV, respectively.

3.2. Coupled system of mechanical/electrical equations

We considered the following set of equations, which couples mechanical and electrical properties of a piezoelectric material:

$$[T] = [c][S] - [e]^T[E] \quad (1)$$

$$[D] = [e][S] + [\varepsilon][E] \quad (2)$$

where [T] is the stress matrix, [S] is the strain matrix, [E] is the electric field vector, [D] is the electric displacement vector, [c] is the elasticity matrix, [ε] is the dielectric constant matrix and [e] is the piezoelectric coefficient matrix. The coupling between piezoelectric and semiconductor physics is introduced by the two matrices [e] and $[e]^T$, which correspond to the direct and inverse piezoelectric effects, respectively.

Electrical equilibrium was described by Poisson's equation:

$$\nabla \cdot D = \rho \quad (3)$$

where ρ is the local density of charge. Considering that ZnO is non-intentionally N-doped, local charge density can be written as:

$$\rho = q.[p - n + N_d^+] \quad (4)$$

where q is the electron charge (in absolute value), n and p are the densities of electrons and holes, and N_d^+ is the density of ionized donor atoms. This equation was used to specify the space charge in the user-defined equations of Comsol Multiphysics®. Volume traps were neglected. Electron and hole concentrations were function of the local electric potential. We used the Boltzmann statistics to describe the free carrier concentrations below degeneracy (around 10^{18} cm^{-3} in ZnO). Dielectric regions were supposed free of charges, with $\rho = 0$.

3.3. Mechanical and electrical boundary conditions

Fig. 2 describes the mechanical and electrical boundary conditions used for a VING unit cell. Mechanical boundary conditions corresponded to a -1 MPa vertical pressure along NW axis, with free vertical and lateral displacement on unit cell top surface, free lateral displacement with forbidden vertical displacement on bottom surface, free lateral and vertical displacement on the outer lateral surface, and free vertical displacement and forbidden lateral displacement on symmetry axis. In terms of electrical boundary conditions, voltage was set to 0 on bottom surface, so as to ensure charge neutrality at the bottom of the doped seed layer. The top surface was equipotential (metal contact), with a voltage V_{top}, which was a result of the simulation.

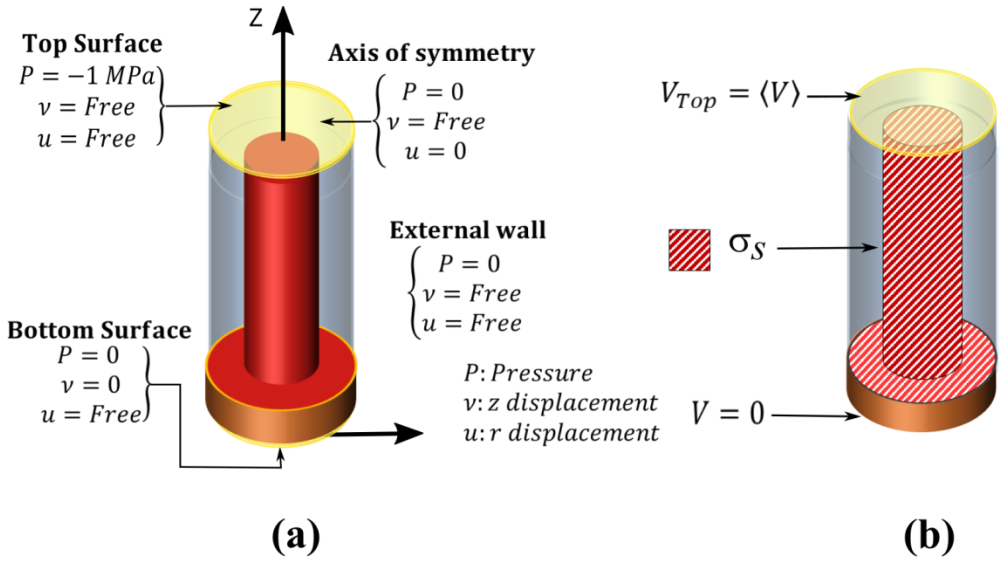

Fig. 2 Mechanical (a) and electrical (b) boundary conditions used for the unit cell.

In contrast with most simulations, a surface charge density σ_s was introduced at all ZnO/PMMA interfaces. This surface charge density depended on the local electric potential. It introduced a discontinuity in the normal component of $\vec{D}$ at ZnO/PMMA interfaces:

$$\vec{n} \cdot \left(\vec{D}_{out} - \vec{D}_{in}\right) = \sigma_s \tag{5}$$

where $\vec{n}$ is the normal to the surface, oriented from inside to outside ZnO. At thermal equilibrium and assuming a uniform traps density (N_{it}) in the gap, σ_s was expressed as a function of local potential V as:

$$\sigma_s = -q^2 N_{it} (V_0 - \varphi_{Fi}) \quad (6)$$

where φ_{Fi} is the difference between Fermi level and intrinsic level in eV and where, in the framework of ultra-slow traps, V_0 is the position dependent potential resulting from the simulation in the initial state (no load). Equation 6 was used to specify the surface charge at the interfaces between the semiconductor material and the dielectric matrix in Comsol Multiphysics®.

4. Results and discussion for O-polar orientation

As explained in the introduction, the presence of surface traps is necessary to explain the significant piezoresponse obtained despite the large doping levels typical of ZnO. The dominant mechanism of radius-dependent piezoresponse degradation is due to the screening of piezoelectric polarization by the free carriers that populate the core of the NW when the radius exceeds the critical radius R_{cr}.[18] In this paper, it is in general assumed that NW radius is smaller than R_{cr}, so as to prevent the formation of a neutral region at the core of the NW, at least in the absence of mechanical load. The aim is to explore the role of NW length and crystal polarity. Focus will be firstly put on O-polar (-c) orientation under compression. The comparison with Zn-polar (+c) orientation will be presented in a second step.

The first observation that emerged from the simulation of the VING cell under compression was that open-circuit voltage V_{OC} saturated for NW lengths larger than a critical value L_{cr} (Fig. 3). Moreover, the saturation voltage depended on NW radius.

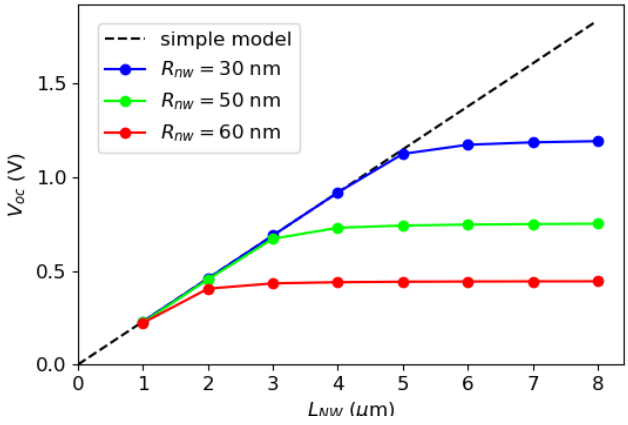

Fig. 3 Evolution of the piezoresponse (V_{OC}) of the VING unit cell as a function of NW length for various values of NW radius R. FEM simulations. O-polar orientation, press action from 0 MPa to -1 MPa, $N_d = 5\times10^{17}$ cm^{-3}.

$N_{it} = 10^{13} eV^{-1} cm^{-2}$. The linear fit (simple model) is consistent with the picture of a purely piezoelectric NW where ZnO is considered insulating, with neither doping nor surface traps.

It was found that piezoresponse saturation was associated with a strong modification of free carriers distribution, with a large density of electrons populating the top of the NW (Fig. 4).

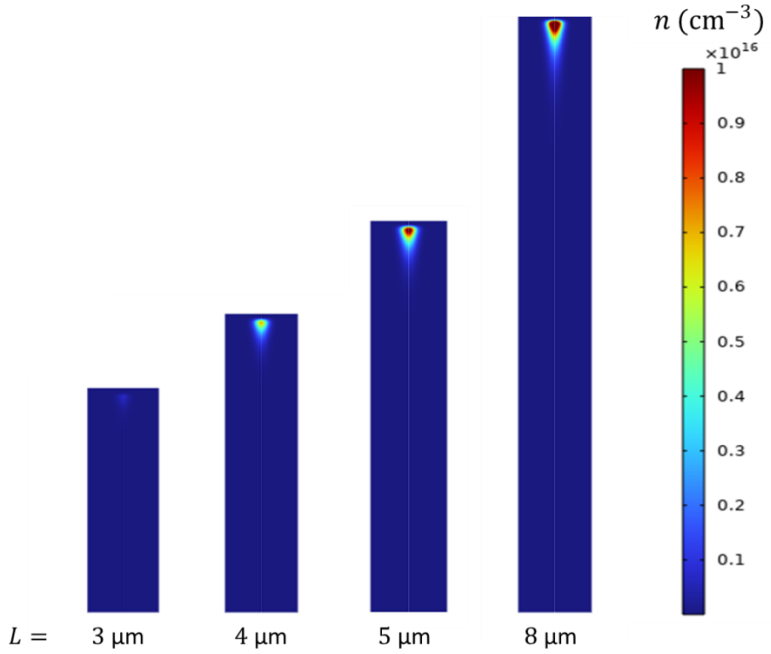

Fig. 4 Typical electron maps under external pressure, obtained with FEM simulations for O-polar orientation. Vertical scale is different from horizontal scale. Focus on the NW region. We considered R = 50nm, L from 3 µm (before piezoresponse saturation) to 8 µm, $N_d = 5 \times 10^{17}$ cm^{-3}, $N_{it} = 10^{13}$ $eV^{-1} cm^{-2}$, press action with final pressure P = - 1MPa. Without pressure, these NWs were fully depleted on their whole length whatever L (not shown).

Our understanding of V_{OC} saturation was the following. With O-polar crystalline orientation, the polarization generated by a vertical compression is oriented against stress direction. Thus, if NW growth direction is defined as z-axis as in Fig. 2, a negative pressure along z creates an upward oriented polarization (refer to Supporting Information for details). Starting from the bottom of the NW, the piezoelectric polarization progressively shifts the electric potential as z increases. At some critical height (L_{cr}), surface traps are not able to deplete NW core any more. Electrons provided either by bottom electrode or by generation-recombination phenomena start to build a neutral region and to screen the piezoelectric potential. Therefore, increasing NW length above this critical height has no effect on the piezoresponse, which then saturates.

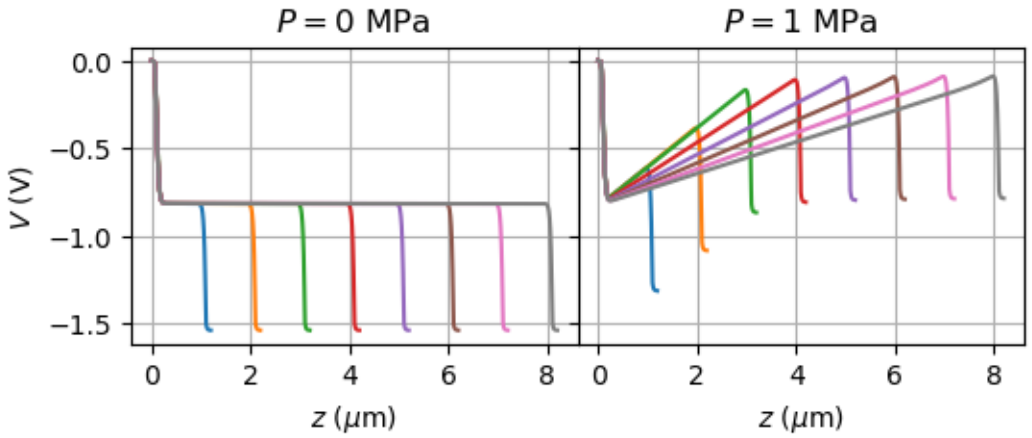

Fig. 5 Electric potential (V) along NW symmetry axis, resulting from FEM simulations, from bottom electrode (z = 0) to top electrode (z = t_{seed} + L + t_{cap}), where t_{seed} = t_{cap} = 0.1 μm. From left to right (blue to grey), L varies from 1 μm to 8 μm by steps of 1 μm, with corresponding colors on the two panels. R = 50 nm, press action from 0 MPa to - 1 MPa. O-polar orientation. Local potential V at position (r,z) is defined with respect to bottom contact.

In order to check this explanation, it is interesting to probe the distribution of the electric potential along NW axis. Fig. 5 shows the electric potential profile V(0,z) along NW symmetry axis (radial coordinate r=0) for different values of L. The reference voltage was taken at the bottom of the seed layer. The voltage on top electrode was independent on L in the absence of mechanical load. It was close to mid-gap on the top electrode, which was expected as Fermi level was pinned close to mid gap for the traps density under consideration (N_{it} = 10^{13} $eV^{-1}cm^{-2}$). Under pressure, V(0,z) increased, so that a positive V_{OC} voltage was generated. The out-of-phase relationship between stress and voltage generation, which is typical of O-polar orientation, was thus verified (stress and voltage having opposite signs). Importantly, V increased linearly with z, with a length-independent slope, until critical height was reached (Fig. 5). For longer than L_{cr} NWs, the voltage still increased linearly with z, but with a smaller slope, the top voltage being fixed to an invariable value. The open-circuit potential V_{OC} is calculated as the difference $V_{top}(P)$-$V_{top}(0)$ where V_{top} is the voltage on top electrode calculated with or without external pressure P. Importantly, it can be observed that V_{OC} was equal to the voltage generated along NW length under pressure.

In order to test the robustness of the explanation of piezoresponse saturation by the formation of a region populated with electrons near the top of the NW, the full depletion approximation was used to derive analytical expressions of critical height L_{cr} and open-circuit voltage V_{OC}. As shown from

simulation (Fig. 5), the voltage drop between bottom contact and NW bottom was unaffected by external pressure. So was the voltage drop between NW top and top contact. Thus, V_{OC} could be evaluated by concentrating on the voltage drop under compression along the sole NW. With a fully depleted NW, strain and polarization could be considered as uniform so that energy bands were subjected to a rigid linear shift in energy along NW axis (refer to Supporting Information for the validation of this assumption by simulation):

$$\phi\,(r,z) = \phi\,(r,0) - \alpha \cdot z \tag{7}$$

where r is the radial distance to NW axis and z is the distance z to the bottom of the NW, and $\phi\,(r,z)$ is the potential energy calculated as the position of the intrinsic level at position (r,z). The electric potential reference was defined by intrinsic level position at the bottom contact (bottom of seed layer), far from surface traps, where charge neutrality is ensured ($n = N_d$). Fig. 6 shows schematic band diagrams along radial direction r, that correspond to z = 0 (NW bottom) and to $z=L_{cr}$ (height at which electron concentration approaches doping level and full depletion approximation becomes invalid).

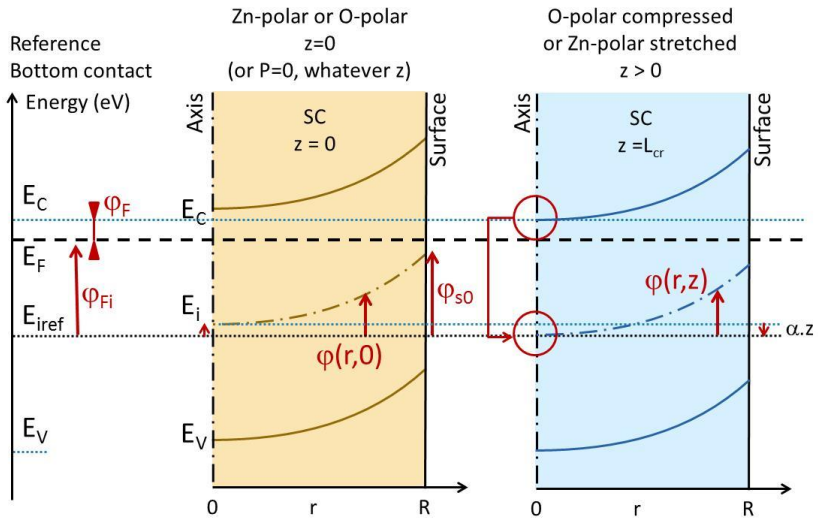

Fig. 6 Schematic band diagram as a function of radial coordinate r at the bottom of the NW and at the critical height L_{cr} where electron concentration approaches doping level on NW axis (r=0). O-polar orientation under compressive stress (P<0). Sign convention = positive electron energy upwards, positive potential downwards. The reference potential E_{iref} is the position of the intrinsic level at the bottom contact, far from surface states. Fermi level is constant (insulating contacts).

It is important to note that, with reference to bottom contact, the band diagram at z = 0 was shifted by $E_i|_{z=0}$ (shift of the intrinsic level between its reference position at bottom contact and its position at z=0), due to the presence of surface traps.

At critical height (L_{cr}) the SC starts to be populated with electrons. This starts near NW axis (r = 0) where potential energy is smaller. According to the band diagrams of Fig. 6, this is realized when

$$\varphi(0, L_{cr}) = -\alpha \cdot L_{cr} = E_i|_{z=0} \tag{8}$$

where $E_i|_{z=0}$ refers to the position of the intrinsic level on NW axis at the bottom of the NW. $E_i|_{z=0}$ is equal to the surface potential φ_s at NW bottom (z=0), decreased by the potential barrier between surface and core. In the case of a fully depleted NW, this writes:

$$E_i|_{z=0} = \varphi(0,0) = \varphi_s|_{z=0} - \frac{qNd}{4\varepsilon} \cdot R^2 \tag{9}$$

where $\varphi_s|_{z=0}$ can be calculated from charge equilibrium between surface traps charge and depleted core at the bottom of the NW:

$$\varphi_s|_{z=0} = \frac{E_g}{2} - \frac{k_B T}{q} \ln \frac{N_c}{N_d} - \frac{N_d}{2N_{it}} \cdot R \tag{10}$$

where E_g is the ZnO bandgap, k_B the Boltzmann constant, T the temperature, q the electron charge (in absolute value), N_c the conduction band density of states. Within the full depletion approximation, L_{cr} would then be:

$$L_{cr} = \frac{-1}{\alpha} \cdot \left[\frac{E_g}{2} - \frac{k_B T}{q} \ln \frac{N_c}{N_d} - \frac{Nd}{2Nit} \cdot R - \frac{qN_d}{4\varepsilon} \cdot R^2 \right] \tag{11}$$

With a simple Hooke's law approach, the coefficient α can be calculated as:

$$\alpha = e_{33} \cdot \frac{P_{NW}}{Y} \cdot \frac{1}{\varepsilon} \tag{12}$$

where P_{NW} is the pressure on top of the NW (negative in compression), Y is the Young's modulus, ε is ZnO permittivity and e_{33} is the piezoelectric coefficient of ZnO along c-axis. It should be noted that, with a ratio between NW radius and NW cell equal to 1/2 and a PMMA resist much more compliant than ZnO, the pressure (P_{NW}) on the NW can be considered as four times that on the cell

(P), in inverse proportion of NW and cell areas. Using the same values as in FEM simulations for ZnO parameters (Y = 210 MPa along c-axis, e_{33} = 1.22 C/m^2, ε = 8.91 ε_0) and P = -1 MPa, α was equal to -2.95×10^5 m/V.

It should be noted that L_{cr} is not an intrinsic parameter as it is inversely proportional to the applied pressure. It decreases as pressure increases, while the saturation V_{OC} value (V_{sat}) is independent of pressure:

$$V_{sat} = -\alpha \cdot L_{cr} = \frac{E_g}{2} - \frac{k_B T}{q} \ln \frac{N_c}{N_d} - \frac{Nd}{2Nit} \cdot R - \frac{qN_d}{4\varepsilon} \cdot R^2 \qquad (13)$$

With the values used for FEM simulations (N_d = 5×10^{17} cm^{-3}, N_{it} = 10^{13} eV^{-1}cm^{-2}), the analytical approximation provided the following values for 50 nm radius: a surface potential $\varphi_s|_{z=0}$ equal to 1.58 eV at NW bottom, a critical length equal to 3.2 µm, and a saturation value for V_{OC} equal to 0.95 V. The theoretical variation of V_{OC} with NW length and radius calculated with this model is plotted in Fig. 7. The abrupt transition between linear operation and saturation was due to the full depletion approximation. However, comparison with Fig. 3 shows that this simple analytical model provided fairly correct orders of magnitude and variation trends.

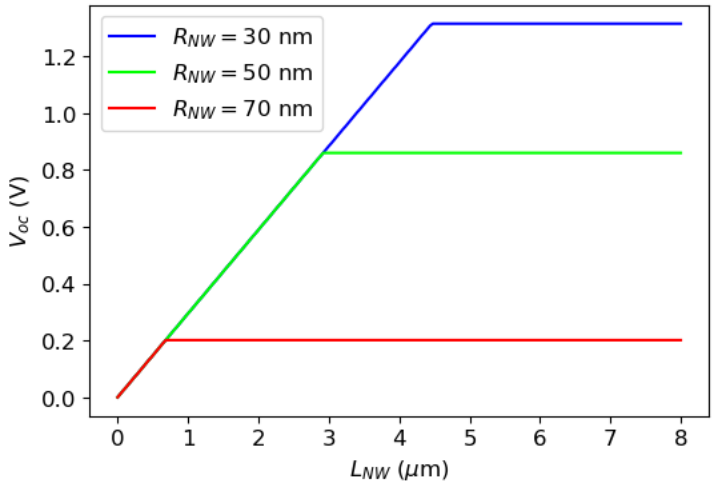

Fig. 7 Evolution of V_{OC} with NW length for different values of NW radius, according to the analytical model. We considered O-polar orientation, N_d = 5×10^{17} cm^{-3} and N_{it} = 10^{13} eV^{-1}cm^{-2}. To be compared with the simulation results of Fig. 3.

Importantly, L_{cr} essentially depended on NW radius and doping density, as well as on surface traps density (Fig. 8). At low doping or for small radius values, the potential profile across the NW was

mostly flat, remaining close to surface potential (see Supporting Information). The L_{cr} dependence to doping level was then dominated by surface potential dependence on N_d. Surface Fermi level being closer to conduction band as doping level increased, a slightly larger NW length was affordable before reaching saturation in narrow NWs. Thus, surface potential position explained the positive slope of $L_{cr}(N_d)$ in Fig. 8(a) and the respective positions of $L_{cr}(R)$ curves for small radius in Fig. 8(b). However, when N_d increased, the band bending across the NW increased in wide NWs, so that there was a smaller margin to shift the potential along z before reaching charge neutrality, and L_{cr} decreased quite steeply. This effect occurred for smaller values of N_d as NW radius was larger. The critical height was thus dependent on R for O-polar compressed NWs (Fig. 8(b)). Finally, the critical height at which a given surface traps density lost control on the potential on NW axis decreased as radius increased. Conversely, the larger was N_{it}, the larger was the potential shift along z required to reach charge neutrality and the larger was L_{cr}, and this, all the more as the NW was thinner (Fig. 8(c)).

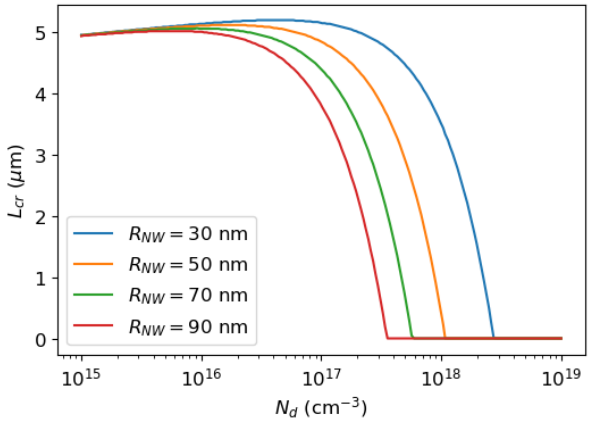

(a)

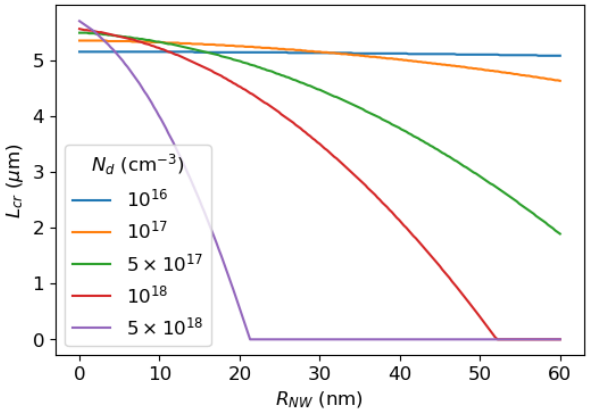

(b)

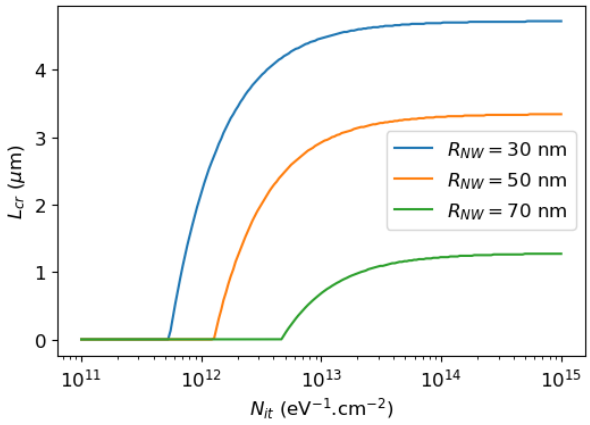

(c)

Fig. 8 Critical length L_{cr} as a function of NW doping level N_d (a), NW radius R (b), and trap density N_{it} (c), obtained with the analytical model for O-polar orientation. Unless otherwise mentioned, we considered $N_d = 5\times10^{17}$ cm^{-3}, $N_{it} = 10^{13}$ eV^{-1}cm^{-2}, R = 50 nm, P = -1 MPa and e_{33} = 1.22 C/m^2. Note that V_{sat} follows the same trends as L_{cr} with N_d, R and N_{it} (equation 13).

5. Influence of crystalline polarity on L-dependent piezoresponse saturation

The influence on polarity on nucleation and growth mechanisms[32] being set apart, the only difference in behavior between O-polar and Zn-polar NWs comes from their opposite polarization. However, this mere difference had a significant impact on piezoresponse under compression. For illustration, Fig. 9 compares the piezoresponse of Zn-polar and O-polar NWs with the same 50 nm radius. The saturation voltage was about twice as large with Zn-polar orientation and the critical height was about 6 µm instead of about 3 µm.

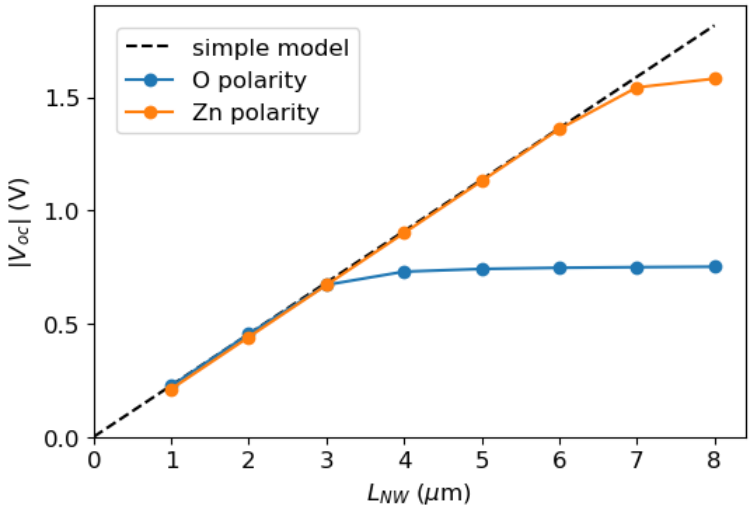

Fig. 9 Comparison of the length-dependent $|V_{OC}|$ saturation obtained with FEM simulations for O-polar and Zn-polar crystalline orientations of the NW in a VING unit cell. Note that V_{OC} is positive with O-polar orientation and negative with Zn-polar orientation. NW radius equal to 50 nm, press action from 0 MPa to -1 MPa.

This was explained by the fact that electric potential varied along NW length in the opposite direction compared to O-polar case. The potential profile was actually the same as for O-polar orientation in the absence of external load but potential was now decreasing (energy potential increased) linearly as axial coordinate z increased (see Supporting Information).

Here, in order to explain saturation, it should be remembered that if potential energy increases with z under axial compression, it is expected that inversion occurs at some height. A large density of holes would then be able to screen further polarization. Due to surface traps and band bending across the NW, inversion would start at NW periphery. This was verified on the holes maps of Fig. 10, where a large density of holes concentrated at the corner of the axisymmetrical representation.

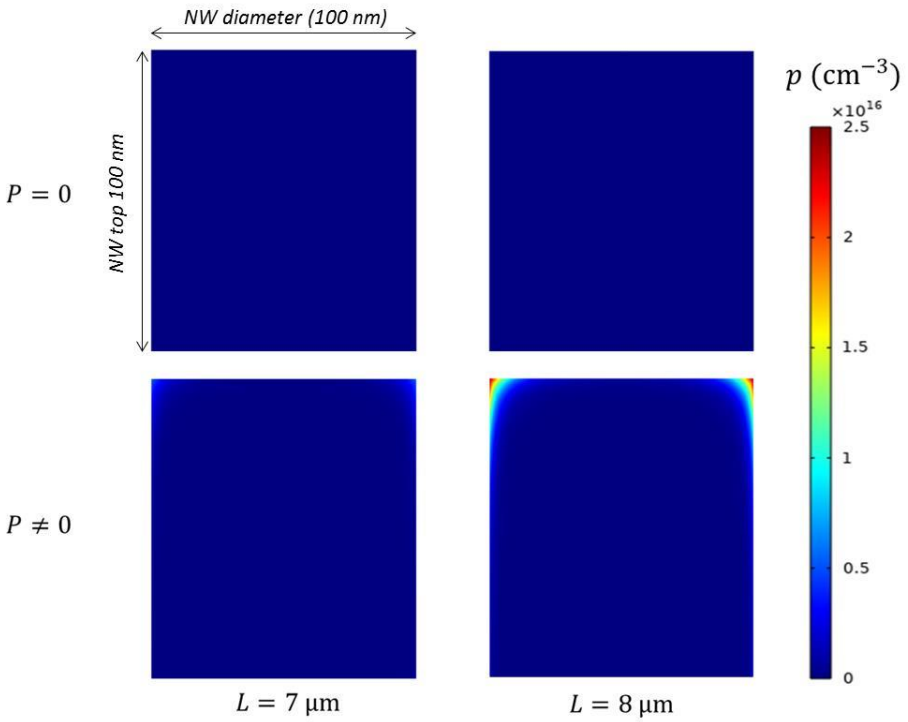

Fig. 10 Holes maps obtained by FEM simulations for Zn-polar orientation (zoom on the upper 100 nm of the NW). R = 50nm, L=7 µm (close to V_{OC} saturation) and L=8 µm (above saturation), $N_d = 5\times10^{17}$ cm^{-3}, $N_{it} = 10^{13}$ eV^{-1}cm^{-2}, press action with P switched from 0 MPa to - 1MPa.

As in previous section, an analytical model was developed in order to support this explanation. With Zn-polar orientation, the band diagrams became those of Fig. 11. As voltage decreased along z, potential energy φ increased and the limit of full desertion was now obtained when inversion was reached at NW periphery (r = R). This was obtained when the valence band was at distance φ_F below Fermi level. From the band diagram of Fig. 11, this resulted in:

$$\varphi(R, L_{cr}) = \varphi_{s0} + \alpha \cdot L_{cr} = \varphi_{Fi} - \varphi_F + \frac{E_g}{2} \tag{14}$$

so that

$$L_{cr} = \frac{1}{\alpha} \cdot \left[\frac{E_g}{2} - \frac{k_B T}{q} \ln \frac{N_c}{N_d} + \frac{Nd}{2Nit} \cdot R\right] \tag{15}$$

where α has the same expression as above but an opposite sign due to opposite polarization ($\alpha = 2.95\times10^5$ m/V). With the same values as above ($N_d = 5\times10^{17}$ cm^{-3}, $N_{it} = 10^{13}$ eV^{-1}cm^{-2},

R = 50 nm, Y = 210 MPa, and P = 1MPa on top of VING cell), the value calculated for L_{cr} was now equal to 5.6µm.

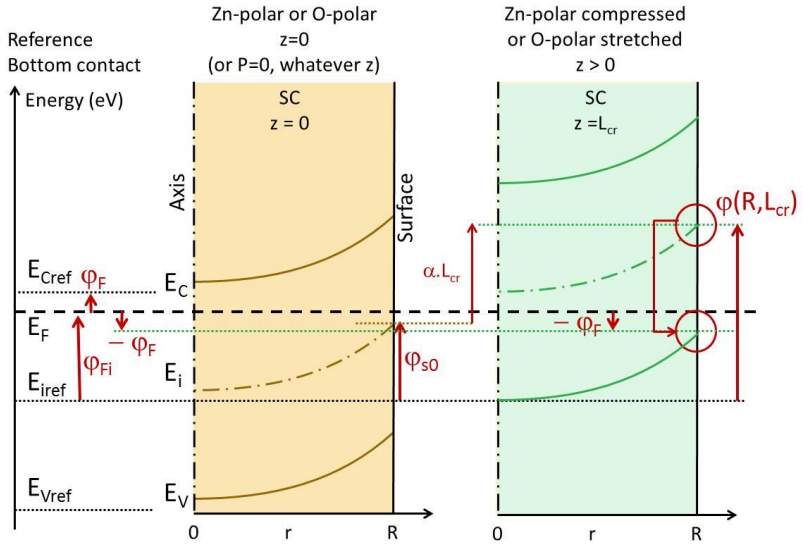

Fig. 11 Schematic band diagram as a function of radial coordinate r at the bottom of the NW and at the critical hight L_{cr} where inversion starts at NW periphery (r = R). Zn-polar orientation under compressive stress (P < 0). Sign convention: positive electron energy upwards, positive potential downwards. The reference potential E_{iref} is the position of the intrinsic level at the bottom contact, far from surface states.

The resulting variations of L_{cr} with doping level, NW radius and surface traps density are shown in Fig. 12. In contrast with the O-polar case, L_{cr} was almost independent of NW radius. The mechanism by which NW radius affected the piezoresponse was essentially the NW core screening by electrons for $R>R_{cr}$, which is a mechanism purely related to SC properties and independent of crystal orientation and mechanical load. Thus, with Zn-polar orientation, there was basically no indirect influence of R on the piezoresponse (as was the case with O-polar orientation, by means of a change of L_{cr} with R).

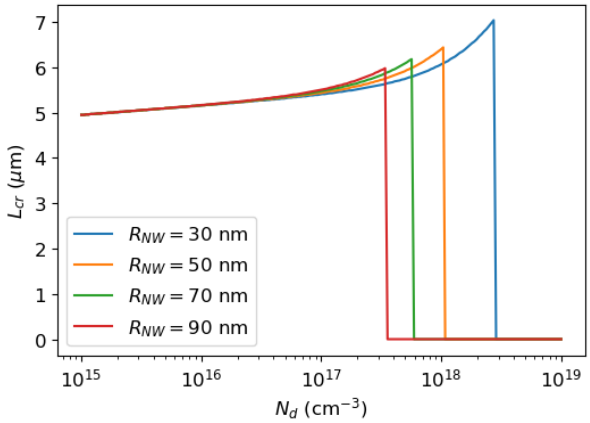

(a)

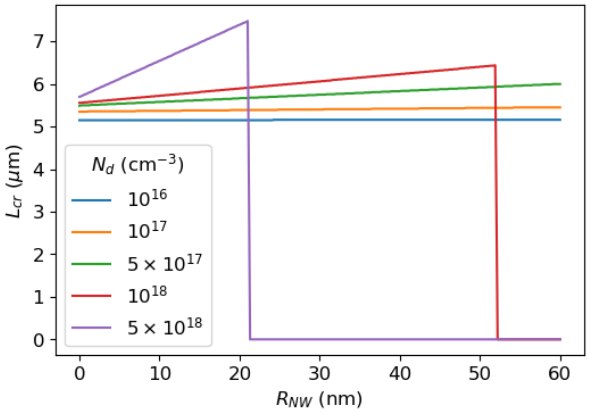

(b)

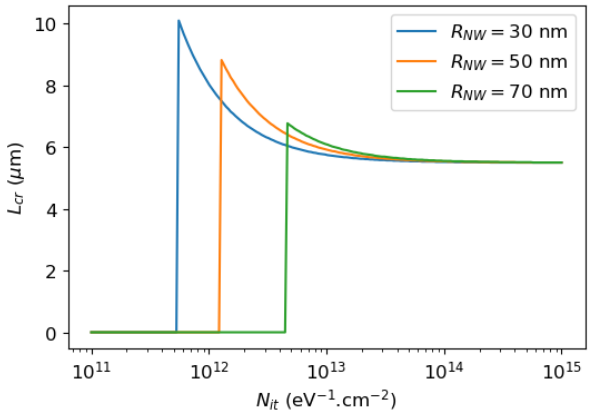

(c)

Fig. 12 Critical length L_{cr} as a function of NW doping level N_d (a), NW radius R (b), and traps density N_{it} (c) calculated with the analytical model, for Zn-polar orientation. Unless otherwise mentioned, we considered $N_d = 5\times10^{17}$ cm^{-3}, $N_{it} = 10^{13}$ eV^{-1}cm^{-2}, R = 50nm, press action from 0 MPa to -1 MPa, Y = 210MPa, $e_{33} = 1.22$ C/m^2. The abrupt drop to 0 corresponds to (R, N_d, N_{it}) conditions which do not fulfill the condition $R<R_{cr}$, even in the absence of pressure (same conditions as in Fig. 8 for O-polar orientation).

With Zn-polar orientation, the saturation potential

$$V_{sat} = -\alpha \cdot L_{cr} \quad (16)$$

was close to mid-gap and hardly dependent on N_d and R (Fig. 13). This analytic conclusion was in fair agreement with the trends obtained from the complete FEM simulation, where the piezoresponse was unaffected by NW radius until the critical radius was reached. With the values used above, the analytical model provided a saturation voltage $V_{sat} = -1.66$ V. Due to the high residual N-type doping of ZnO, the absolute value of voltage shift required to reach inversion was

larger than that required to start to accumulate electrons. This explained why $|V_{sat}|$ was larger for compressed Zn-polar NWs than for compressed O-polar NWs.

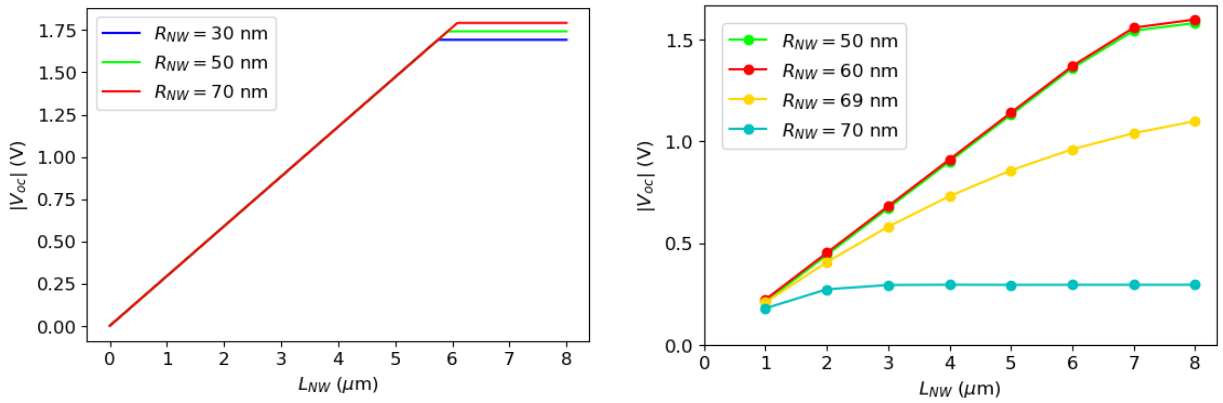

(a) (b)

Fig. 13 Variation of the absolute value of V_{OC} as a function of NW length for Zn-polar orientation. Plots obtained from analytical expressions (a) and from FEM simulations (b). For radius values smaller than critical radius R_{cr}, V_{OC} was mostly independent of R with both approaches (R_{cr} value being equal to about 80 nm under full depletion approximation and to slightly below 69 nm according to FEM simulation). Above R_{cr}, the V_{OC} degradation obtained with FEM simulations was not due to the presence of holes at the upper periphery of the NW but to the presence of electrons at the bottom of the NW.

It should be noted that with the usual VING structure, which features a conducting contact at the bottom and an insulating contact on top, electron supply by the bottom contact allows the NW to be easily populated with electrons – whether at the bottom core above R_{cr} or above L_{cr} below R_{cr}. In contrast, there is no such a reservoir for holes. Therefore, the growth of the holes populated region at NW periphery above L_{cr} relies only of the availability of generation-recombination processes with associated time constants. This may explain why larger V_{OC} values can be reached experimentally during the piezoelectric transients in the presence of PN junctions that shift the bands to higher energies and where saturation would be expected to result from screening by holes.[28] It can be noted that the experimental values of V_{OC} obtained experimentally in [27] were in the range of 0.43V, 0.66V and 1.32V for NW lengths of 2.3µm, 3.9µm and 5.9µm, respectively. It is difficult to make a rigorous comparison with our results in the absence of precise information about stress, radial dimensions or the role of the CuSCN passivation layer on interface properties. Nonetheless, these results are reasonably consistent with present work.

6. R-dependence of critical length and impact on piezoresponse R-dependent transition

It has been observed in a previous paper that the R-dependent transition between the high piezoresponse regime (for small radii) and a small piezoresponse regime (for large radii) featured a different steepness depending on crystal polarity.[21] This difference is illustrated in Fig. 14. For this figure, and contrary to [21], the same values of doping level and traps density were used for both polarities, in order to isolate the influence of geometry. The values of R_{cr} above which the R-dependent degradation of piezoresponse occurs were thus the same for the two polarities. Until now, R_{cr} has been used to set the limit between the high piezoresponse regime (with a fully depleted NW) and the low piezoresponse regime (with free electrons populating the center of the NW and screening the piezopotential).[18] However, it is clear from Fig. 14 that the R-dependent transition is affected by crystal polarity.

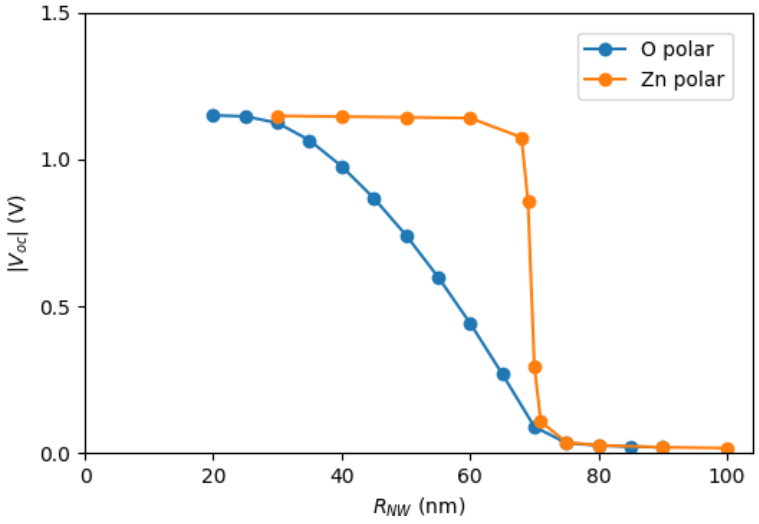

Fig. 14 Comparison of $|V_{OC}|$ dependence with NW radius depending on crystal polarity, as obtained from FEM simulations. We considered L = 5 µm, $N_d = 5\times10^{17}$ cm^{-3}, $N_{it} = 10^{13}$eV^{-1} cm^{-2} and press action from 0 MPa to -1 MPa.

The above-mentioned mechanisms of L-dependent saturation can explain this difference. Indeed, the critical height L_{cr} above which surface traps lose control on NW depletion was found to depend on R for compressed O-polar NWs, while it was mostly independent of R for Zn-polar orientation. Thus, the dominant mechanisms behind piezoresponse dependence on geometry were different. With O-polar orientation, saturation started for rather small values of L, and was dominated by the

decrease of L_{cr} with radius (see Fig. 3). This resulted in an early degradation of the saturation voltage as R increased. The approach of critical radius was only slightly visible by a change in the initial slope of the $V_{OC}(L)$ curve for R=60nm, but it came into play while the L-dependent saturation was already very strong. In contrast, the saturation value was mostly independent of R with Zn-polar orientation (see Fig. 13). Piezoresponse degradation was much sharper. It started only when NW radius exceeded critical radius, with an associated degradation of $V_{OC}(L)$ slope. With Zn-polar orientation, the dominant mechanisms was thus a direct R-dependent degradation, with little role of L_{cr}. In order to obtain a large piezoresponse from SC VING devices, it is thus necessary to keep NW radius below R_{cr} in all cases, but the L_{cr} related degradation introduces an even stricter condition for O-polar orientation, due to L_{cr} dependence with R.

7. Influence of external pressure

Finally, it should be noted that L_{cr} values depended on the external pressure, and so did V_{OC} values – as long as L_{cr} was not reached. Larger L_{cr} values were affordable for lower compression. Thus, even though, for a given external pressure, saturation is expected for a certain L_{cr} value, it may be interesting to use longer NWs in order to get some sensitivity to lower pressures (Fig. 15)

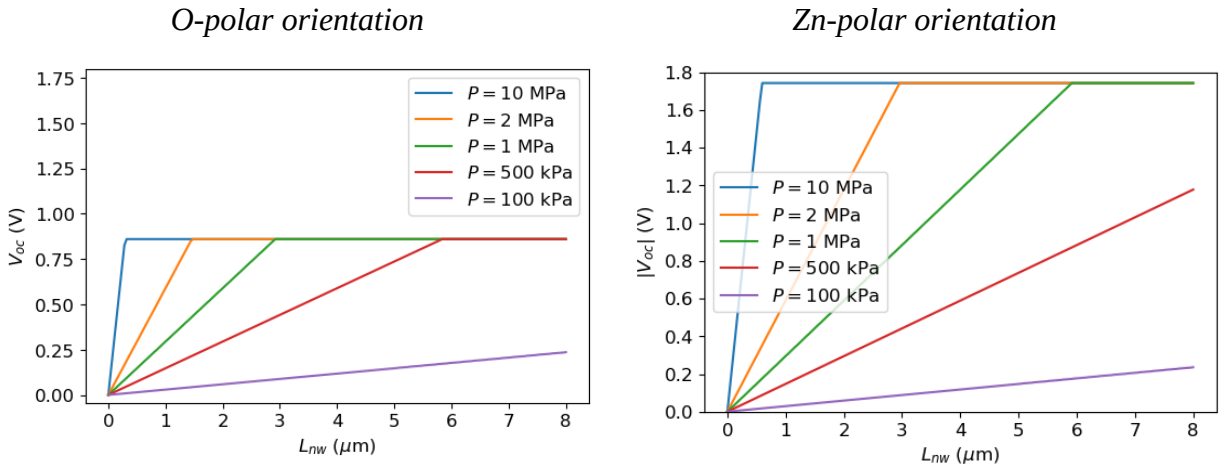

Fig. 15 Influence of external pressure on the length dependence of V_{OC}, according to the analytical model. We considered R = 50nm, $N_d = 5\times10^{17}\,cm^{-3}$, $N_{it} = 10^{13}\,eV^{-1}cm^{-2}$, and a press action from 0 MPa to -1 MPa.

8. Conclusions

To conclude, we carried out a theoretical study of the piezoresponse of SC NW-based piezoelectric devices. We used the ZnO VING configuration as a support example for such a device. It was shown that the control of electron depletion by surface traps *along the whole NW length* was essential to guarantee significant piezoresponse. A necessary condition was to keep NW radius below the critical radius R_{cr} that ensures NW depletion in the absence of any external stress and is independent of crystal polarity. However, we also demonstrated the importance of NW length, which entails the V_{OC} saturation when above a certain (pressure and radius-dependent) length L_{cr}. The order of magnitude of L_{cr} was in the range of several micrometers, *i. e.* in the range of experimental values. This effect is thus meaningful in terms of applications. The mechanism behind this saturation was explained in terms of the linear shift of conduction and valence bands along NW length, which resulted from strain-induced piezoelectric polarization. This shift was sufficient to drive the upper portion of the SC NW in accumulation or in inversion, depending on NW polarity. Above a certain height, electrons started to populate the core of O-polar axially compressed NWs, while holes populated the periphery of Zn-polar NWs. Based on this understanding, a simple analytical model was derived to calculate V_{OC} dependence with NW geometry, crystal polarity and external pressure. This model was based on the full depletion approximation in cylindrical coordinates and provided fair agreement with accurate FEM simulations. It allowed us to explore the respective roles of geometry, crystal polarity, doping level, surface traps density and external pressure. It also explained why O-polar NWs featured a smoother R-dependent transition than Zn-polar NWs, between negligible and large V_{OC} values, when R decreased. It was shown that, below the critical radius R_{cr}, Zn-polar NWs switched almost directly to the theoretical value expected for a fully depleted NW. The situation was different for O-polar NWs. While the depletion condition was fulfilled at the bottom of the NW for radius smaller than Rcr, it was not necessary fulfilled at the top of the NW. The length-dependent saturation was bringing an additional limitation to the piezoresponse. To reach the maximum piezoresponse, which corresponds to the fully depleted NW, it was necessary to deplete the whole NW, and thus to get out of the length-dependent saturation region. This was achieved for radii smaller than R_{cr}, thus leading to a much smoother transition for O-polar orientation. It should not be forgotten that the role of polarity would be inversed for axial stretching, with larger piezoresponse and steeper transition for O-polar than for Zn-polar orientation. Moreover, the general trends obtained with V_{OC} can be extrapolated to the piezoelectric

coefficient d_{33}. Finally, the methodology and the results obtained here with ZnO can be easily extended to other materials. The analytical expressions derived in this paper should provide a useful support for the analysis of piezoelectric experiments on SC NW-based structures and for the optimization of devices based on these structures. As long as NW geometry is more easily controlled and measured than doping level and surface traps density, these expressions can also be used to evaluate the order of magnitude of the values achieved by a technology for the latter parameters, by monitoring the degradation of V_{OC} with NW radius and its saturation with NW length.

Acknowledgements

This work has been partly supported by the ANR projects SCENIC (under grant agreement ANR-20-CE09-0005) and LATINO (under grant agreement ANR-21-CE50-0026) from the French Ministry of Research. It has also been partly supported by the project PULSE-COM of the European Union's Horizon 2020 Research and Innovation programme under grant agreement n°863227.

References

[1] H. Wei, H. Wang, Y. Xia, D. Cui, Y. Shi, M. Dong, C. Liu, T. Ding, J. Zhang, Y. Ma, An overview of lead-free piezoelectric materials and devices, J. Mater. Chem. C, Vol. 6, pp. 12446–12467, https://doi-org./10.1039/C8TC04515A (2018)

[2] M. Safaei, H.A. Sodano, S.R. Anton, A review of energy harvesting using piezoelectric materials: state-of-the-art a decade later (2008-2018), Smart. Mater. Struct., Vol. **28,** no. 113001, pp. 1-62, https://doi.org/10.1088/1361-665X/ab36e4 (2019)

[3] Ü. Özgür, Ya. I. Alivov, C. Liu, A. Teke, M. A. Reshchikov, S. Doğan, V. Avrutin, S.-J. Cho, and H. Morkoç, A comprehensive review of ZnO materials and devices, Journal of Applied Physics, Applied Physics Reviews, Vol. 98, n° 041301, https://10.1063/1.1992666 (2005)

[4] A. J. Lopez Garcia, G. Sico, M. Montanino, V. Defoor, M. Pusty, X. Mescot, F. Loffredo, F. Villani, G. Nenna, G. Ardila, Low-Temperature Growth of ZnO Nanowires from Gravure-Printed ZnO Nanoparticle Seed Layers for Flexible Piezoelectric Devices, Nanomaterials, Vol. 11, Issue 6, Article n°1430, 15 pages, https://doi.org/10.3390/nano11061430 (2021)

[5] R. Liu, Z.L. Wang, K. Fukuda, T. Someya, Flexible self-charging power sources. Nature Reviews Materials, Vol. 7, pp. 870–886, https://doi.org/10.1038/s41578-022-00441-0 (2022)

[6] A. J. Lopez Garcia, R. Tao, M. Mouis, G. Ardila, A New Approach to Calculate the Piezoelectric Coefficient of Piezo-Semiconductor Nanowires Integrated in Nanocomposites: Experiment and Simulation, IEEE Transducers Conference Proceedings, pp. 1056-1059, https://doi.org/10.1109/TRANSDUCERS50396.2021.9495621 (2021)

[7] S. Xu, Y. Qin, C. Xu, Y. Wei,R. Yang, Z.L. Wang, Self-powered nanowire devices, Nature Nanotechnology, Vol. 5, pp. 366-373, https://doi.org/10.1038/NNANO.2010.46 2010)

[8] E. Lee, J. Park, M. Yim, Y. Kim, G. Yoona, Characteristics of piezoelectric ZnO/AlN_2 stacked flexible nanogenerators for energy harvesting applications, Applied Physics Letters, Vol. 106, n° 023901, https://doi.org/10.1063/1.4904270 (2015)

[9] M. Bah, T. Slimani Tlemcani, S. Boubenia, C. Justeau, N. Vivet, J.-M. Chauveau, F. Jomard, K. Nadaud, G. Poulin-Vittrant and D. Alquier, Assessing the electrical activity of individual ZnO nanowires thermally annealed in air, Nanoscale advances, Vol. 4, pp. 1125-1135, https://doi.org/10.1039/D1NA00860A (2022)

[10] T. Cossuet, F. Donatini, A. M. Lord, E. Appert, J. Pernot, V. Consoni, Polarity-dependent high electrical conductivity of ZnO nanorods and its relation to hydrogen, Journal of Physical Chemistry C, Vol. 122, pp. 22767-22775, https://doi.org/10.102/acs.jppc.8b07388 (218)

[11] A.R. Hutson, Piezoelectricity and conductivity in ZnO and CdS, Physical Review Letters, Vol. 4, n°10, pp 505-507, https://doi.org/10.1103/PhysRevLett.4.505 (1960)

[12] T. Ogawa, H. Oikawa, A. Kojima, Decrement of piezoelectric constants caused by screening effect of conduction electrons on the effective charge of CdS crystals, Japanese Journal of Applied Physics, Vol. 10, n°5, https://doi.org/10.1143/JJAP.10.593 (1971)

[13] D. A. Scrymgeour, J. W. P. Hsu, Correlated, piezoelectric and electrical properties in individual ZnO nanorods, Nano Letters, vol. 8, n°8, pp. 2204-2209, https://doi.org/10.1021/nl080704n (2008)

[14] A. Waseem, A. Abdulla, I. V. Bagal, J.-S. Ha, J. K. Lee and S.-W. Ryu, Self-powered and flexible piezo-sensors based on conductivity controlled GaN nanowire-arrays for mimicking rapid- and slow-adapting mechanoreceptors, npj Flexible Electronics, Vol. 6, no. 58, https://doi.org/10.1038/s41528-022-00197-1 (2022)

[15] C.H. Wang, W.S. Liao, Z.H. Lin, N.J. Ku, Y.C. Li, Y.C. Chen, Z.L. Wang, C.P. Liu, Optimization of the output efficiency of GaN nanowire piezoelectric nanogenerators by tuning the free carrier concentration, Adv. Energy Mater. Vol. 4, pp. 1–7. https://doi.org/10.1002/aenm.201400392 (2014).

[16] M. Riaz, J. Song, O. Nur, Z.L. Wang, M. Willander, Study of the piezoelectric power generation of ZnO nanowire arrays grown by different methods, Adv. Funct. Mater. 21 628–633. https://doi.org/10.1002/adfm.201001203 (2011).

[17] O. Synhaivskyi, D. Albertini, P. Gaffuri, J.-M. Chauveau, V. Consonni, B. Gautier, and G. Bremond, Evidence of Piezoelectric Potential and Screening Effect in Single Highly Doped ZnO:Ga and ZnO:Al Nanowires by Advanced Scanning Probe Microscopy, J. Phys. Chem. C, Vol. 125, pp.15373-15383, https://doi.org/10.1021/acs.jpcc.1c00926 (2021)

[18] R. Tao, M. Mouis, G. Ardila, Unveiling the influence of Surface Fermi Level Pinning on the Piezoelectric Response of Semiconducting Nanowires, Advanced Electronic Materials, Vol. 4, Issue 1, Article no. 1700299, https://doi.org/10.1002/aelm.201700299 (2018)

[19] R. Calarco, T. Stoica, O. Brandt and L. Geelhaar, Surface-induced effects in GaN nanowires, J. Mater. Res., Vol. 26, no. 17, pp. 2157-2168, https://doi.org/10.1557/jmr.2011.211 (2011)

[20] A. J. Lopez Garcia, M. Mouis, A. Cresti, R. Tao, G. Ardila, Influence of slow or fast surface traps on the amplitude and symmetry of the piezoelectric response of semiconducting-nanowire-based transducers, Journal of Physics D: Applied Physics, Vol. 55, no. 405502, 13pp, https://doi.org/10.1088/1361-6463/ac8251 (2022)

[21] A. J. Lopez Garcia, M. Mouis, V. Consonni, G. Ardila, Dimensional Roadmap for Maximizing the Piezoelectrical Response of ZnO Nanowire-Based Transducers: Impact of Growth Method, Nanomaterials, Vol. 11, Issue 4, n° 941, https://doi.org/10.3390/nano11040941 (2021)

[22] M. Ghini, N. Curreli, M. B. Lodi, N. Petrini, M. Wang, M. Prato, A. Fanti, L. Manna, I. Kriegel, Control of electronic band profiles through depletion layer engineering in core–shell nanocrystals, Nature Communications, Vol. 13, no. 537, https://doi.org/10.1038/s41467-022-28140-y (2022)

[23] A. Waseem, M. A. Johar, A. Abdullah, I. V. Bagal, J.-S. Ha, J. K. Lee, S.-W. Ryu, Enhanced performance of a flexible and wearable piezoelectric nanogenerator using semi-insulating

GaN:Mg/ZnO coaxial nanowires, Nano Energy, Vol. 90, n° 106552, https://doi.org/10.1016/j.nanoen.2021.106552 (2021)

[24] N. Gogneau, P. Chrétien, T. Sodhi, L. Couraud, L. Leroy, L. Travers, J.-C. Harmand, F. H. Julien, M. Tchernychevaa and F. Houzé, Electromechanical conversion efficiency of GaN NWs: critical influence of the NW stiffness, the Schottky nano-contact and the surface charge effects, Nanoscale, Vol. 14, pp.4965-4976, https://doi.org/10.1039/d1nr07863a (2022)

[25] A. J. Lopez Garcia, T. Jalabert, M. Pusty, V. Defoor, X. Mescot, M. Montanino, G. Sico, F. Loffredo, F. Villani, G. Nenna, G. Ardila, Size and semiconducting effects on the prizoelectric performances of ZnO nanowires grown onto gravure-printed seed layers on flexible substrates, Nanoenergy advances, Vol. 2, pp. 197-209, https://doi.org/10.3390/nanoenergyadv2020008 (2022)

[26] T. Jalabert, M. Pusty, M. Mouis and G. Ardila, Investigation of the diameter-dependent piezoelectric response of semiconducting ZnO nanowires by Piezoresponse Force Microscopy and FEM simulations, Nanotechnology, under review (2022)

[27] Q. He, X. Li, J. Zhang, H. Zhang, J. Briscoe, P-N junction-based ZnO wearable textile nanogenerator for biomechanical energy harvesting, Nano Energy, Vol. 85, n°105938 (9 pages), https://doi.org/10.1016/j.nanoen.2021.105938 (2021)

[28] M. A. Johar, A. Waseem, M. A. Hassan, J.-H. Kang, J.-S. Ha, J. K. Lee, S.-W. Ryu, Facile growth of high aspect ratio c-axis GaN nanowires and their application as flexible p-n NiO/GaN piezoelectric nanogenerators, Acta Materialia, Vol. 161, pp. 237-245 https://doi.org/10.1016/j.actamat.2018.09.030 (2018)

[29] G. Romano, G. Mantini, A. di Carlo, A. d'Amico, C. Falconi and Z. L. Wang, Piezoelectric potential in vertically aligned nanowires for high output nanogenerators, Nanotechnology, Vol. 22, n° 465401, pp. 1-6, https://doi.org/10.1088/0957-4484/22/46/465401 (2011)

[30] R. Tao, M. Parmar, G. Ardila, P. Oliveira, D. Marques, L. Montès, M. Mouis, Performance of ZnO based piezo-generators under controlled compression, Semiconductor Science and Technology, Vol. 32, no. 6, Special Issue on Piezotronics, doi:10.1088/1361-6641/aa691f, hal-01986533 (2017)

[31] R. Tao, R. Hinchet, G. Ardila, L. Montès, M. Mouis, Evaluation of the Vertically Integrated NanoGenerator performances in flexion, Journal of Physics Conference Series, PowerMEMS Conference, Vol. 476, no. 12006, https://doi.org/10.1088/1742-6596/476/1/012006 (2013)

[32] V. Consonni, A. M. Lord, Polarity in ZnO nanowires: A critical issue for piezotronic and piezoelectric devices, Nano Energy, Vol. 83, no. 105789 33 pages, https://doi.org/10.1016/j.nanoen.2021.105789 (2021)

Length and polarity dependent saturation of the electromechanical response of piezoelectric semiconducting nanowires

Supporting Information

Andrés Jenaro Lopez Garcia, Mireille Mouis, Thomas Jalabert, Alessandro Cresti, Gustavo Ardila

Univ. Grenoble Alpes, CNRS, Grenoble INP, IMEP-LaHC, F-38000 Grenoble, FRANCE
E-mail: mouis@minatec.grenoble-inp.fr, ardilarg@minatec.grenoble-inp.fr

S1. Critical radius for full depletion

In the limiting case of a very high density of surface traps with a uniform distribution in the bandgap, the critical radius can be evaluated analytically using Poisson's equation in a fully depleted cylinder:

$$R_{cr} = \frac{\varepsilon}{q\pi N_{it}}\left[-1+\sqrt{1+\frac{4\pi^2 q N_{it}^2}{\varepsilon N_d}\cdot\varphi_{Fi}(N_d)}\right] \quad \text{(Eq. S1)}$$

where q is the electron charge (in absolute value), ε is the SC permittivity, N_d the doping level, N_{it} the surface charge density and φ_{Fi} Fermi level position with respect to intrinsic level.

$$\phi_{Fi} = \frac{E_g}{2} - \frac{k_B T}{q}\cdot\ln\frac{N_c}{N_d} \quad \text{(Eq. S2)}$$

where E_g is the SC bandgap, k_B Boltzmann constant, T the temperature, and N_c the conduction band density of states. The critical radius depends on doping level and surface traps density (Fig. S1). The full depletion approximation provides slightly optimistic values but correct trends.

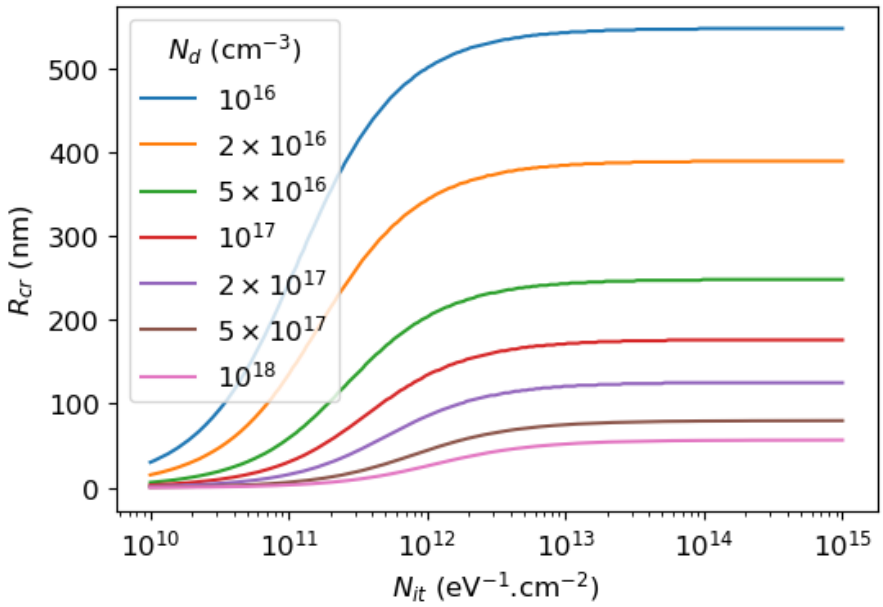

Fig. S1. Critical radius under the full depletion approximation in cylindrical coordinates as a function of surface density of states (N_{it}) and NW doping level (N_d).

S2. Crystal orientation

Vertically grown III-N and ZnO NWs have a preferential orientation along the c-axis, with m-plane facetted walls. Two polarities can be found, one along [0001] also named +c or Zn-polar, and one along $[000\bar{1}]$ also named -c or O-polar. These 2 polarities are non-equivalent. An axial compression along the c-axis generates a piezoelectric polarization that is opposite to the applied force for O-polar orientation and collinear to the applied force for Zn-polar orientation.

S3. Mechanical and piezoelectric parameters used in the simulations

Table S1: Mechanical and semiconducting properties of ZnO used in numerical simulations

ZnO property	Symbol	Value	References
Elastic constants	C_{11} C_{12} C_{13} C_{33} C_{44} C_{66}	209.7 GPa 121.1 GPa 105.1 GPA 210.9 GPa 42.47 GPa 42.29 GPa	Bateman et al., Journal of Applied Physics 1962, doi:10.1063/1.1931160
Piezoelectric coefficients	e_{13} e_{33} e_{15}	-0.51 C/m^2 1.22 C/m^2 -0.45 C/m^2	Carlotti et al.. Appl. Phys. Lett. 1987, doi:10.1063/1.98502

Relative dielectric constants	ε_{11} ε_{33}	7.77 8.91	Ashkenov et al. Journal of Applied Physics 2003, doi:10.1063/1.1526935.
Band gap	E_g	3.37 eV	Look et al. Solid State Communications 1998, doi:10.1016/S0038-1098(97)10145-4
Conduction and valence band density of states	N_c N_v	$3.68\times10^{24}m^{-3}$ $1.13\times10^{25}m^{-3}$	From electron and hole density of states mass taken from Fan et al., Journal of nanoscience and nanotechnology 2005, doi:10.1166/JNN.2005.182.
Intrinsic carrier density	n_i	2.1×10^{-10} cm^{-3}	$n_i = \sqrt{N_v N_c} e^{-E_g/2k_B T}$ where k_B is the Boltzmann constant and T the temperature

S4. Example of device meshing

Due to the large aspect ratio of the structure, it is impossible to display the full meshing. The following figure shows an example of realization with zooms on the top and on the bottom of the nanowire.

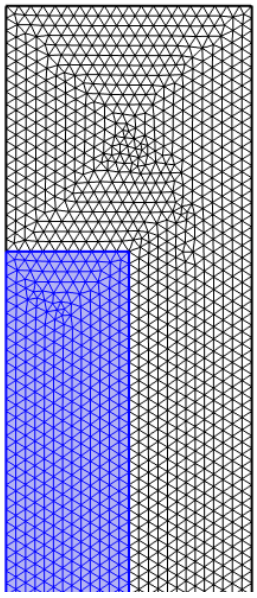

(a) Zoom on top of NW

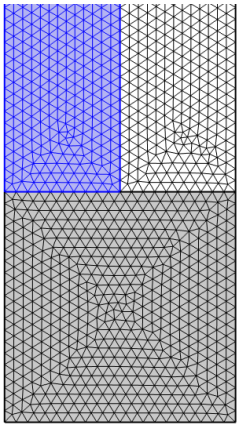

(b) Zoom on seed layer and bottom of NW

Fig. S2. Example of meshing for NW radius and length equal to 50nm and 3µm, respectively. For each zoom, the horizontal and vertical scales are the same. The NW is in blue.

S5. Energy band shift along NW axis under axial compression

Fig. S3 plots the electric potential across a 60nm radius NW at different heights along the NW (z coordinate). These curves were obtained from FEM simulations for O-polar orientation. The curve at z=0 was partly influenced by the surface traps density on the top surface of the seed layer, through 3D effects. Except from that, the simulation confirmed that the radially-dependent band diagram could be considered as linearly shifted downwards as a whole (towards positive voltage, negative potential energy), as z increased.

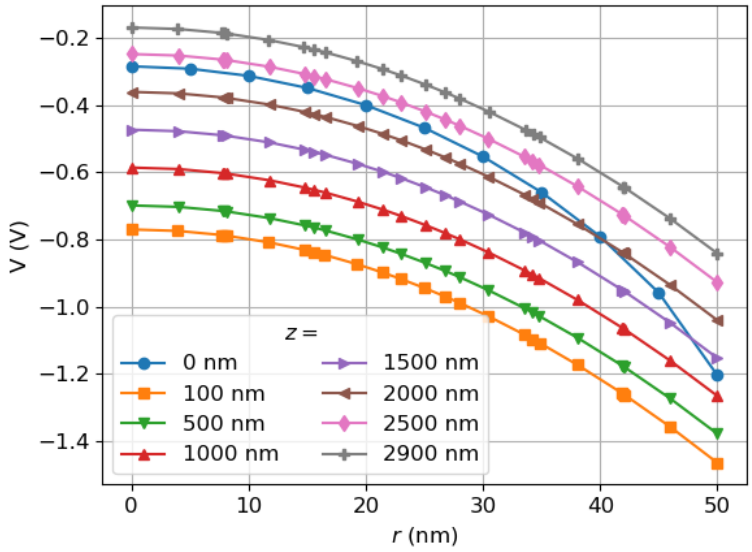

Fig. S3. Electric potential across the NW at different positions z, as obtained from FEM simulations, for O-polar orientation. We considered R = 50 nm, $N_d = 5\times10^{17}$ cm^{-3}, $N_{it} = 10^{13}$ $eV^{-1}cm^{-2}$, L = 3 µm (before saturation). Here, z=0 corresponds to NW bottom (top of seed layer).

S6. Influence of doping level on radial potential variation

Under the full depletion approximation, energy bands are parabolic across the NW and their curvature is equal to $qN_d/4\varepsilon$. Fig. S4 shows the influence of NW doping level.

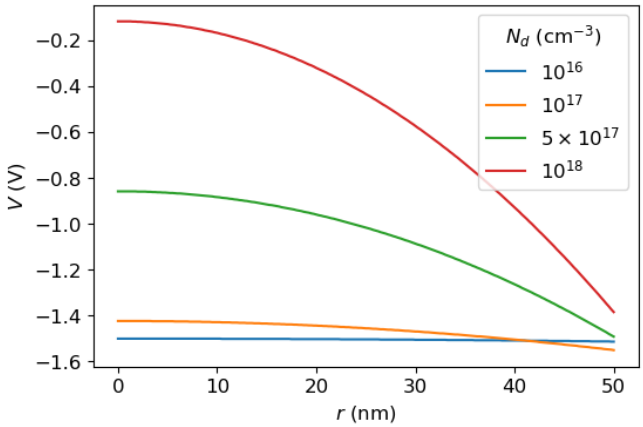

Fig. S4. Influence of doping level on the radial variation of electric potential across the NW, as obtained from the analytical model for an unstrained NW with O-polar or Zn-polar orientation (independent of crystal polarity). We considered R = 50 nm. Nit = 10^{13} $eV^{-1}cm^{-2}$.

S7. Zn-polar orientation: electric potential profiles along NW axis

With Zn-polar orientation, the electric potential decreased along z in an axially compressed VING structure, as shown in Fig. S5. As with O-polar orientation, the voltage drop across the seed layer and across the cap layer could be considered as independent of pressure so that V_{OC} could be evaluated by concentrating on the voltage drop in the compressed NW.

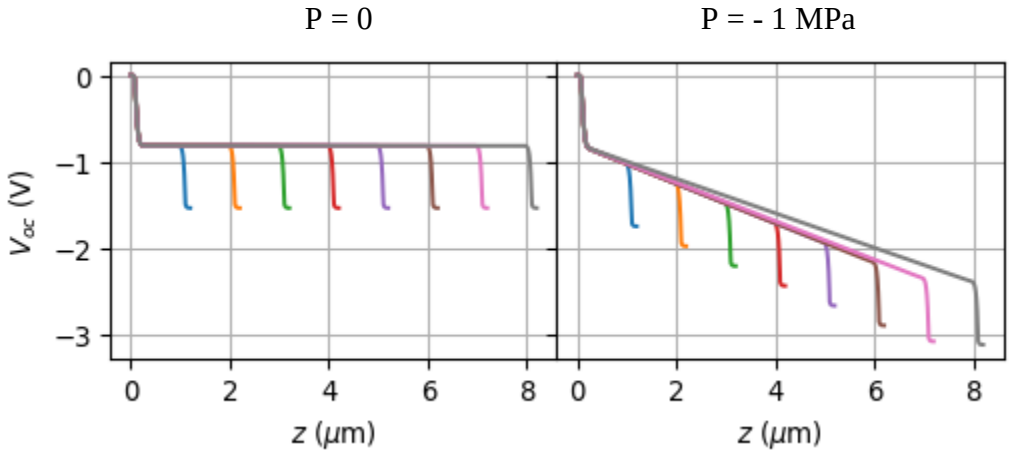

Fig. S5. Electric potential along the symmetry axis of Zn-polar NWs, before and after mechanical loading with pressure P, and for different values of NW length. From left to right (blue to grey), L varies from 1 µm to 8 µm by steps of 1 µm, with corresponding colors on the two panels. We considered R = 50 nm, N_d = 5×10^{17} cm^{-3}, Nit = 10^{13} $eV^{-1}cm^{-2}$. Zn-polar orientation.

S8. Influence of NW radius on electron distributions for Zn-polar and O-polar orientations

In order to confirm that the V_{OC} degradation obtained for R values of 69nm and 70nm with FEM simulation is effectively due to the fact that these R values are above critical radius, Fig. S6 displays electron maps, which show that above 69nm, the NW core begins to be populated with electrons, starting from NW bottom, as surface traps are unable to fully deplete the NW.

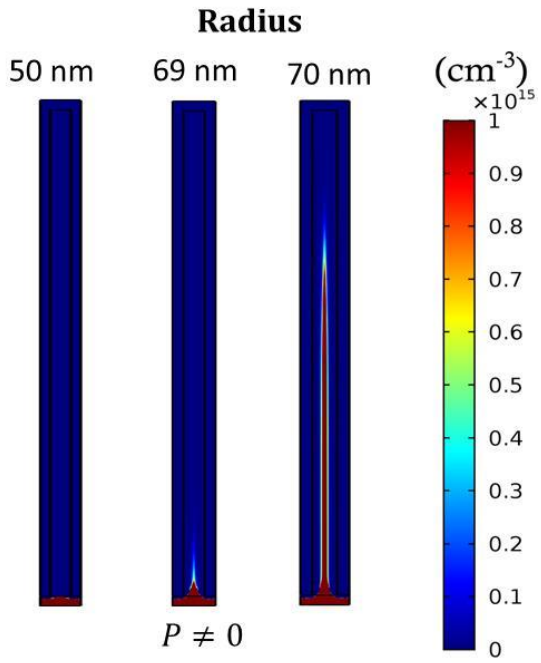

Fig. S6. Influence of NW radius on the electron concentration maps for Zn-polar orientation. We considered L=5µm (below critical height L_{cr}), $N_d = 5\times10^{17}$ cm^{-3}, $N_{it} = 10^{13}$ $eV^{-1}cm^{-2}$ and P = - 1 MPa.

With O-polar orientation, NW radius influenced electron distribution below critical radius, as a result of polarization-induced band shift (Fig. S7). The electron population grew near the top of the NW above the critical height L_{cr} – where L_{cr} decreased as R increased.

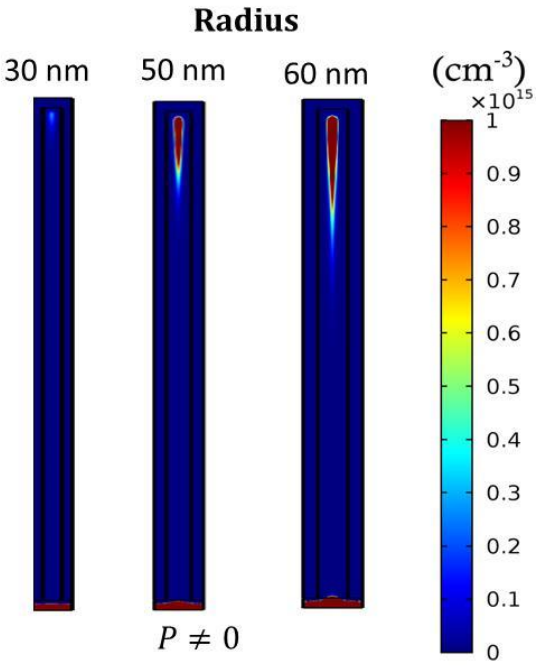

Fig. S7. Influence of NW radius on the electron concentration maps for O-polar orientation. We considered L=5μm (above critical height L_{cr}), $N_d = 5\times10^{17}$ cm^{-3}, $N_{it} = 10^{13}$ $eV^{-1}cm^{-2}$ and P = - 1 MPa.